INTERNATIONAL JOURNAL FOR NUMERICAL METHODS IN FLUIDS
Int. J. Numer. Meth. Fluids **31**: 661–680 (1999)

THE NUMERICAL SIMULATIONS OF EXPLOSION AND IMPLOSION IN AIR: USE OF A MODIFIED HARTEN'S TVD SCHEME

T.G. LIU, B.C. KHOO* AND K.S. YEO

Department of Mechanical and Production Engineering, National University of Singapore, 10 Kent Ridge Crescent, Singapore 119260, Singapore

SUMMARY

Numerical simulations of explosion and implosion in air are carried out with a modified Harten's TVD scheme. The new scheme has a high resolution for contact discontinuities in addition to maintaining the good features of Harten's TVD scheme. In the numerical experiment of spherical explosion in air, the second shock wave (which does not exist in the one-dimensional shock tube problem) and its subsequent implosion on the origin have been successfully captured. The positions of the main shock wave, the contact discontinuity and the second shock wave have shown satisfactory agreement with those predicted from previous analysis. The numerical results are also compared with those obtained experimentally. Finally, simulations of a cylindrical explosion and implosion in air are carried out. Results of the cylindrical implosion in air are compared with those of previous work, including the interaction of the reflected main shock wave with the contact discontinuity and the formation of a second shock wave. All these attest to the successful use of the modified Harten's TVD scheme for the simulations of shock waves arising from explosion and implosion. Copyright © 1999 John Wiley & Sons, Ltd.

KEY WORDS: TVD scheme; second shock wave; radially symmetric flow

1. INTRODUCTION

Theoretical and experimental studies of spherical blast waves have been considered over the past decades by several researchers (Boyer [1], Brode [2], Friedman [3], Glass [4], Bake [5]). When a highly pressurized sphere is suddenly released, an inward rarefaction wave in the high-pressure region is generated. At the same time, a main shock wave moves out through the low-pressure region and a contact discontinuity appears between the rarefaction wave and the shock wave. Furthermore, experiments [1,4] have shown that the resulting flow for this problem is quite complex and a second shock wave can arise between the contact discontinuity and the rarefaction wave.

The formation of the second shock wave as deduced from the results of the analysis by Boyer [1] and Friedman [3] can be summarized as follows. The high-pressure gas, through a spherical rarefaction wave, must expand to a lower pressure than that reached by an equivalent one-dimensional expansion. Unlike a one-dimensional shock tube problem, no steady state region exists between the tail of the rarefaction wave and the main shock wave because of the

* Correspondence to: Department of Mechanical and Production Engineering, National University of Singapore, 10 Kent Ridge Crescent, Singapore 119260, Singapore.

CCC 0271–2091/99/200661–20$17.50

Received August 1996
Revised January 1998

flow three-dimensionality. The pressure immediately behind the main shock front decreases with time, resulting in the generation of expansion waves that are able to overtake the main shock front and cause it to attenuate. With the decrease of strength of the main shock wave, the velocity immediately behind the main shock wave decreases. This implies that at the earlier time of the explosion, the maximum velocity is at the tail of the rarefaction wave; at the same time, the minima pressure and density also occur there. It is at the position of maximum velocity, which is located at the tail of rarefaction wave, that the flow evolves into a discontinuity—the second shock wave. For more details, the reader may want to refer to the original references [1,3].

Because the second shock wave occurs in the expanding region, it is expected to be rather weak initially and propagate outwards with the expanding gas. However, its strength increases with time and reaches a fairly high intensity in a short time. Soon, the second shock wave stops propagating outwards and comes to a halt before reverting backwards to implode on the origin.

The contact discontinuity initially moves out behind the main shock front but with a decreasing velocity. After a certain time, the contact discontinuity, following the moving-in flow as induced by the converging second shock wave, ceases its outward motion and begins to move in towards the origin. After its implosion at the center, the second shock wave moves out and interacts with the incoming contact discontinuity; then it propagates through the contact surface. The interaction causes the contact discontinuity to move slightly outwards in the radial direction again. At the same time, an inward rarefaction wave is 'generated' at the point of interaction. According to analysis [1,3], following this inward rarefaction wave there is a third shock wave, albeit a weak one, as the situation is very similar to that required for the formation of the second shock wave. Experiments [1,4], however, did not reveal the presence of the third shock wave mentioned above. This can possibly be attributed to the third shock wave being relatively much weaker and occurring so late that it is extremely difficult to detect it. In fact, the existing discontinuities in the flow are weak and the whole flow region is nearly uniform before the arrival of the third shock wave.

Some numerical experiments have also been carried out for this kind of explosion problem. In 1981, Flores and Holt [6] employed Glimm's scheme to compute the explosion generated by a pressurized sphere in water. It was found [7], however, that there are difficulties associated with the use of Glimm's scheme to compute the rarefaction region near to the explosion center after the rarefaction wave has reached the origin. This could be one reason why the computation was not carried out long enough for the rarefaction wave to reach the explosion center, as in Flores and Holt's work. In another study, Charrier and Tessieras [8] numerically simulated a cylindrical explosion in air by using a front-tracking technique. However, they did not show the presence of the second shock wave as the computation was again not performed for a sufficiently long time.

In a more recent development, Falcovitz and Birman [9] employed the GRP/ST method, which is a variant of the singularities tracking GRP method developed earlier by Ben-Artzi and Falcovitz [10], and studied its tracking properties of both strong and weak discontinuities as applied to the simplified one-dimensional compressible duct flow. Indeed, there was good agreement of results. On the other hand, because the GRP/ST method involves the use of an extra moving grid system to track the discontinuities and a cell-merging/cell-splitting mechanism is employed to circumvent the formation of free small cells that invariably result in extremely small time step sizes, the method is rather complex, and extension to multi-dimensional flows can be very computer intensive. The availability of the simpler high-order TVD or ENO schemes, which are well-established, robust and capable of fine resolution of

shock capturing as discussed below, is the preferred method for the present simulation of an explosion/implosion in air. The extension to simulation of multi-dimensional/multi-medium flow, as in an underwater explosion in future work is also greatly facilitated.

There are very few satisfactory experiments for the implosion problem. Because it is extremely difficult to break a spherical diaphragm instantaneously, experiments by Boyer [1] and Glass [4] failed to show the essence of a spherical implosion, such as the implosion of the main shock wave and the interaction of the reflected main shock wave with the contact discontinuity. However, numerical simulations by Sod [11] for this kind of problem showed that a main shock wave moves inwards with increasing strength, imploding on the origin and being reflected from it. After that, the main shock wave interacts with the radially incoming contact discontinuity, resulting in the propagation and further reflection of the main shock, hence creating a moving-in second shock wave.

The high-resolution TVD [12] and ENO [13,14] schemes developed by Harten and co-workers have been extensively used to deal with the Euler and Navier–Stokes equations. Numerical experiments have shown that these schemes are reasonably robust. On the other hand, the direct application of the TVD or ENO schemes to compressible flow problems may result in the 'smearing' of the contact discontinuities at a rate $O(n^{1/(p+1)})$ [15], where p is the order of accuracy of the scheme used and n is the number of the time steps. To overcome this problem, Harten introduced the concept of subcell resolution and proposed a method named ENO/SR [16]. Subsequently, Mao [17] introduced a discontinuity capturing technique by merging with Harten's subcell resolution to 'sharpen' the contact discontinuity. Both Harten's ENO/SR and Mao's methods perform extremely well for one-dimensional planar flows. Attempts to extend the ENO/SR method to higher dimensions using operator splitting were, however, not so successful [14]. Thus far, a multi-dimensional version of ENO/SR has yet to be developed. In another parallel effort, Yang [18] combined the ENO scheme with a slope modification technique, which is an artificial compression method (ACM) type technique pioneered by Harten [19], to increase the resolution of contact discontinuities. Yang's method is simple enough but some adjustable parameters inherent in his method have to be determined with numerical experiments. In general, it can be reckoned that a scheme coupled with the judicious use of an ACM technique will largely increase the resolution in the region near to the contact discontinuity and yet will not change the properties and attributes of the original scheme. The indiscriminate use of artificial compression throughout may distort the solution in smooth regions [19]. Therefore, the ACM technique can enhance and benefit the overall numerical computation if its application is restricted to the immediate region of the contact discontinuity. Partly based on this motivation, a version of Harten's TVD scheme, which is coupled to the ACM technique for application to the contact discontinuity, is adopted in this work. The authors seek to use this modified Harten's TVD scheme to simulate both explosion and implosion problems in air. The physical phenomena of the second shock wave in a spherical explosion predicted analytically [2] and observed experimentally [1,4] will be carefully compared with the computed results. Furthermore, the case of cylindrical explosion in air is simulated under the same initial conditions as the spherical explosion, and the associated discontinuity curves for both spherical and cylindrical explosions are discussed. For the implosion problem, the results of the shock wave imploding at the origin, and the propagation and reflection at the contact discontinuity, are compared with previous numerical work that employed other numerical schemes. The present study will serve as an important starting point for future work in the simulation of an underwater explosion, where data, whether experimental or theoretical, are even more limited for the purpose of comparison. Extension to multi-dimensional flow for the study of an underwater explosion in the presence of a nearby free-surface is the ultimate objective.

This paper is organized as follows. In Section 2, the Euler equations for a one-dimensional, radially symmetric inviscid flow are described and the system of equations at the origin is presented. In Section 3, a modified Harten's TVD scheme is constructed and the numerical method used to handle the singularity at the origin is discussed. In Section 4, the modified Harten's TVD scheme is applied to track the evolution of a spherical explosion and its numerical results are compared with previous work. Also in Section 4, computations of the cylindrical explosion and implosion are carried out and discussed. A concluding summary is given in Section 5.

2. THE GOVERNING EQUATIONS

The one-dimensional equations of motion for an inviscid, non-heat conducting, radially symmetric flow are usually written in the form

$$\frac{\partial U}{\partial t}+\frac{\partial F(U)}{\partial r}=W(U), \tag{2.1}$$

where

$$U=\begin{pmatrix}\rho\\ \rho u\\ E\end{pmatrix}, \qquad F(U)=\begin{pmatrix}\rho u\\ \rho u^2+p\\ (E+p)u\end{pmatrix}, \qquad W(U)=-\frac{\alpha-1}{r}\begin{pmatrix}\rho u\\ \rho u^2\\ (E+p)u\end{pmatrix}. \tag{2.2}$$

Equations (2.1) and (2.2) are in non-dimensional form (details of the non-dimensionalization are given in Section 4). The independent variables are time (t) and radial distance from the center of the explosion (r). The dependent dimensionless variables are density (ρ), radial velocity (u), pressure (p) and total energy per unit volume (E). In Equation (2.2), $\alpha=2$ for cylindrical flow and 3 for spherical flow. For closure of Equation (2.1), the state equation of a perfect gas is used and given as

$$E=\frac{p}{\gamma-1}+\frac{1}{2}\rho u^2, \tag{2.3}$$

where γ is the ratio of specific heats, equal to 1.4 for air. Equation (2.1) can also be rewritten in another conservative form,

$$\frac{\partial \tilde{U}}{\partial t}+\frac{\partial F(\tilde{U})}{\partial r}=S(\tilde{U}), \tag{2.4}$$

where

$$\tilde{U}=r^{\alpha-1}U, \qquad S(\tilde{U})=\frac{\alpha-1}{r}\begin{pmatrix}0\\ \tilde{p}\\ 0\end{pmatrix}, \quad \tilde{p}=r^{\alpha-1}p. \tag{2.5}$$

One may observe that the right-hand-side term of Equation (2.4) is always positive. Numerical experiments have indicated that a positive right-hand-side term tends to enhance numerical stability. Furthermore, due to the continuity of $S(\tilde{U})$ through the material contact surface, Equation (2.4) is the preferred form for the simulation of multi-fluid flow.

There is a potential problem in solving Equations (2.1) or (2.4) directly due to the singularity at $r = 0$; this singularity can be removed. The following form of the conservative equations is adopted to ensure that the resulting finite difference numerical scheme employed is compatible with the original PDE at the origin. At the origin,

$$\frac{\partial \rho}{\partial t} + \alpha \frac{\partial \rho u}{\partial r} = 0, \tag{2.6a}$$

$$\frac{\partial E}{\partial t} + \alpha \frac{\partial (E+p)u}{\partial r} = 0 \tag{2.6b}$$

and

$$u = 0. \tag{2.6c}$$

3. A MODIFIED TVD SCHEME: NUMERICAL IMPLEMENTATION

A high-order TVD or ENO scheme possesses rather unique features, such as high-resolution for shock capturing without oscillations, and is commonly used for the simulation of compressible flow. To further enhance the resolution of the contact discontinuity and ensure the stability of computations for a long period of time, the authors propose the use of a modified Harten's TVD scheme with the incorporation of the ACM technique for the immediate region of the contact discontinuity. The form of the new scheme for Equation (2.4) is

$$\tilde{U}_j^{n+1} = \tilde{U}_j^n - \xi_r (H_{j+1/2}^n - H_{j-1/2}^n) + \frac{1}{2}\Delta t S(\tilde{U}_j^{n+1}) + \frac{1}{2}\Delta t S(\tilde{U}_j^n); \tag{3.1}$$

$$H_{j+1/2}^n = \frac{1}{2}(F(\tilde{U}_j^n) + F(\tilde{U}_{j+1}^n) + r_{j+1/2}^{\alpha-1} G_{j+1/2}^n), \quad G_{j+1/2}^n = R_{j+1/2}\Phi_{j+1/2}^n; \tag{3.1a}$$

$$\Phi_{j+1/2}^n = (\phi_{j+1/2}^1, \phi_{j+1/2}^2, \phi_{j+1/2}^3)^T; \tag{3.1b}$$

$$\phi_{j+1/2}^l = \frac{1}{\xi_r}(g_j^l + g_{j+1}^l - \sigma(\xi_r \lambda_{j+1/2}^l + \gamma_{j+1/2}^l)\alpha_{j+1/2}^l), \quad l = 1, 2, 3; \tag{3.1c}$$

$$g_j^l = (1 + q_{j+1/2}^l) g_j^{H,l}, \quad l = 1, 2, 3; \tag{3.1d}$$

$$g_j^{H,l} = \min \ \mathrm{mod}(\sigma(\xi_r \lambda_{j-1/2}^l)\alpha_{j-1/2}^l, \sigma(\xi_r \lambda_{j+1/2}^l)\alpha_{j+1/2}^l), \quad l = 1, 2, 3; \tag{3.1e}$$

$$q_{j+1/2}^l = S_{j+1/2} \times \frac{|\alpha_{j+1/2}^l - \alpha_{j-1/2}^l|}{|\alpha_{j+1/2}^l| + |\alpha_{j-1/2}^l|} \times \frac{\varphi(\xi_r \lambda_{j+1/2}^l)}{\sigma(\xi_r \lambda_{j+1/2}^l)}, \quad l = 1, 2, 3; \tag{3.1f}$$

$$S_{j+1/2} = \frac{1}{2}\left|\mathrm{sign}(\lambda_{j+1/2}^2 - \lambda_{j-1/2}^2) - \mathrm{sign}(\lambda_{j+1/2}^3 - \lambda_{j-1/2}^3)\right|; \tag{3.1g}$$

$$\gamma_{j+1/2}^l = \begin{cases} \dfrac{g_{j+1}^l - g_j^l}{\alpha_{j+1/2}^l} & \text{if } \alpha_{j+1/2}^l \neq 0 \\ 0 & \text{otherwise} \end{cases}, \quad l = 1, 2, 3; \tag{3.1h}$$

$$(\alpha_{j+1/2}^1, \alpha_{j+1/2}^2, \alpha_{j+1/2}^3)^T = R_{j+1/2}^{-1} \Delta_{j+1/2} U, \qquad \Delta_{j+1/2} U = U_{j+1} - U_j, \quad l = 1, 2, 3; \tag{3.1i}$$

$$\varphi(x) = \begin{cases} |x| & \text{if } |x| \geq 2\varepsilon \\ \dfrac{x^2 + 4\varepsilon^2}{4\varepsilon} & \text{otherwise} \end{cases}, \qquad \sigma(x) = \frac{1}{2}\varphi(x) - \frac{1}{2}x^2; \tag{3.1j}$$

$$\min \mod(x, y) = \begin{cases} \operatorname{sign}(x) \min(|x|, |y|) & \text{if } xy > 0 \\ 0 & \text{otherwise} \end{cases}. \tag{3.1k}$$

Here, n and j are the indices of the time and radial distances respectively; $\xi_r = \Delta t/\Delta r$, where Δt and Δr are the time and spatial step sizes respectively; $R_{j+1/2}$, $R^{-1}_{j+1/2}$ and $\lambda^l_{j+1/2}$ are the right eigenvectors, the left eigenvectors and the eigenvalues of the matrix $\partial F/\partial U$ respectively; and $\lambda^1 = u$. For the computation, the following CFL condition is adopted:

$$\frac{\Delta t}{\Delta r} \max(|u| + c) \leq \text{CFL}, \tag{3.2}$$

which is set to 0.8 in the present work, with $\varepsilon = 0.2$.

One may observe that the scheme presented above is very similar to Harten's TVD scheme for Equation (2.4) except for the expression in Equation (3.1d), where $q^l_{j+1/2}$, is set equal to zero for the latter. The construction of $q^l_{j+1/2}$ is based on Harten's ACM techniques [12,15,19] with the following general fact: the two non-linear eigenvalues, λ^2 and λ^3, exhibit opposite trends across the contact discontinuity along the radial direction, i.e. if one increases, the other must decrease across the contact discontinuity. This is unlike the respective changes across the shock or rarefaction wave region, where both eigenvalues either decrease or increase along the radial direction. It is believed that the opposite trends for λ^2 and λ^3 across the contact discontinuity give rise to a *relatively* larger amount of numerical viscosity in the affected region as compared with other regions, and this can lead to 'smearing' of the contact discontinuity. To decrease the inordinate increase of the said numerical viscosity, $S_{j+1/2}$ given in Equation (3.1g) is first evaluated to detect the presence of the contact discontinuity and the ACM technique is then applied directly on the affected region to ensure a 'sharp' contact discontinuity. The ACM technique is simple and involves only marginally more computation.

For a system of linear Euler equations, Harten [12] had earlier shown that Harten's TVD scheme is generally both conservative and second-order. In a similar fashion, the present modified Harten's scheme can be shown to possess the above mentioned properties, which are provided in Appendix A. Furthermore, the present scheme is considered to be TVD under the CFL condition $\Delta t/\Delta r \max(|u| + c) \leq ((5 - \sqrt{17})/2)$. The CFL condition presented here is more severe than Harten's TVD scheme. Numerical tests, however, show that the total variation (TV) is bounded and essentially oscillation-free under the less restrictive $\text{CFL} \leq 0.95$. In the numerical implementation, for the purpose of expediency, a larger time step according to $\text{CFL} = 0.8$ was used and checks were periodically made according to the stricter CFL condition, with differences in the results of only about 3%. Furthermore, since there is no entropy consideration for a linearly degenerate field—the contact discontinuity [12]—the entropy property of the original Harten's TVD scheme is maintained.

The governing equations valid at the origin as reflected in Equation (2.6) are discretized as follows:

$$\rho_0^{n+1} = \rho_0^n - \alpha \frac{\Delta t \rho_0^n (4u_1^n - u_2^n)}{2\Delta r}, \tag{3.3a}$$

$$E_0^{n+1} = E_0^n - \alpha \frac{\Delta t (E_0^n + p_0^n)(4u_1^n - u_2^n)}{2\Delta r}, \tag{3.3b}$$

$$p_0^{n+1} = (\gamma - 1)E_0^{n+1}, \tag{3.3c}$$

$$u_0^{n+1} = 0. \tag{3.3d}$$

Here, '1' and '2' indicate that the variables are evaluated at the respective grid points $r_1 = \Delta r$ and $r_2 = 2\Delta r$, and '0' refers to the variable taken at the origin.

Figure 1(a) and (b) show the density profiles, computed with the standard Harten's TVD and the present scheme respectively, for a shock tube problem with the same initial conditions of $p_H = 4.0$, $\rho_H = 4.0$, $u_H = 0.0$, $p_L = 1.0$, $\rho_L = 1.0$ and $u_L = 0.0$. If the two density profiles are plotted in one figure, the two curves will fully coincide except at the contact discontinuity region, where the grid points are reduced from eight nodal points for Harten's TVD scheme to three nodal points for the present scheme. Both schemes employed the same number of total nodal points for representation and a constant $\Delta x = 0.01$ throughout. The resolution of the contact discontinuity has improved while other regions remain unaffected. This also shows that the ACM technique affects only the locality of the contact discontinuity region, as was intended in this shock tube problem. In the next section, the contact discontinuity is always exhibited as a fairly sharp interface, which is computed as an unsteady problem for a long period of time.

4. RESULTS AND DISCUSSIONS

4.1. Numerical simulation of explosion in air

For purposes of comparison, the authors use the test model that has been analyzed by Brode [2] and investigated experimentally by Boyer [1]. A sphere with initial radius $r'_0 = 2$ in., containing the compressed air at pressure $p'_H = 326$ psi and at a temperature $T'_0 = 299$ K, is assumed to be surrounded by air at pressure $p'_0 = 15$ psi and the same temperature. The symbol prime ($'$) denotes dimensional quantity. In this case, the dependent variables are non-dimensionalized via $\rho = \rho'/\rho'_0$, $p = p'/\rho'_0 a'^2_0$ and $u = u'/a'_0$. Here, a'_0 is the sonic speed and is given by $a'^2_0 = \gamma(p'_0/\rho'_0)$. The physical independent variables, t' and r', are made non-dimensional using $4r'_0/a'_0$ and $4r'_0$ respectively. Hence, the relationship between the physical time t' and the non-dimensional time t is $t' = 293t$ (μs), and the non-dimensional initial parameters are $p_H = 15.514$, $\rho_H = 21.7333$, $u_H = 0$, $p_0 = 0.715$, $\rho_0 = 1.0$ and $u_0 = 0$.

In Figure 2(a)–(c) the pressure profiles at different physical times are shown. In Figure 2(a) the second shock front can only be discerned from the pressure profiles at about $t' = 120$ μs. At an earlier time of 85 μs, the shock can be detected from the temperature profiles at the non-dimensional radial position of about 0.42 (see Figure 3(a)–(c) for the plots of the temperature profiles). Detecting the presence of the second shock wave numerically is not so distinct and easy before 85 μs. This is because the second shock wave before that time is rather weak. Therefore, its exact position will be obtained based on the more objective criterion of the position of minimum pressure or temperature near the tail region of the rarefaction wave. The basis of this criterion stems from the fact that, at early times, the second shock wave occurs at the tail of the rarefaction wave, where the minima of pressure and temperature are located. In Figure 2(a), at about 60 μs, the rarefaction wave reaches the origin and results in a rapid decrease of pressure; in another 80 μs time period (i.e. at $t' = 140$ μs), the pressure at the origin would be lower than that at the tail of the rarefaction wave. From that moment of about $t' = 140$ μs till the time when the second shock wave arrives at the center, the pressure, density and temperature between the origin and the second shock wave are constant along the radial

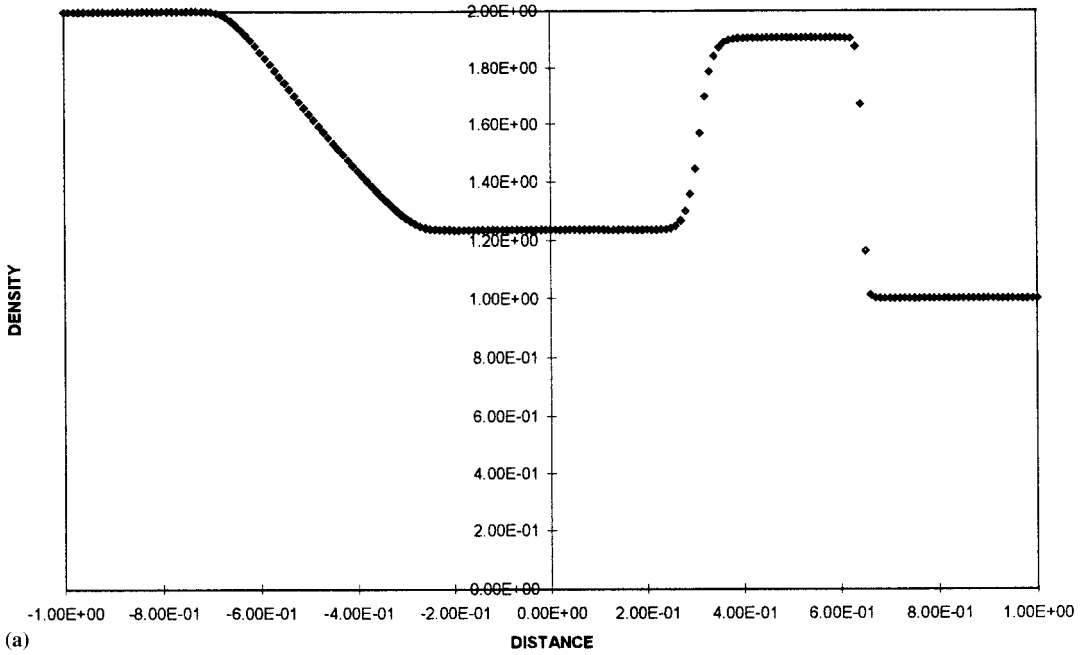

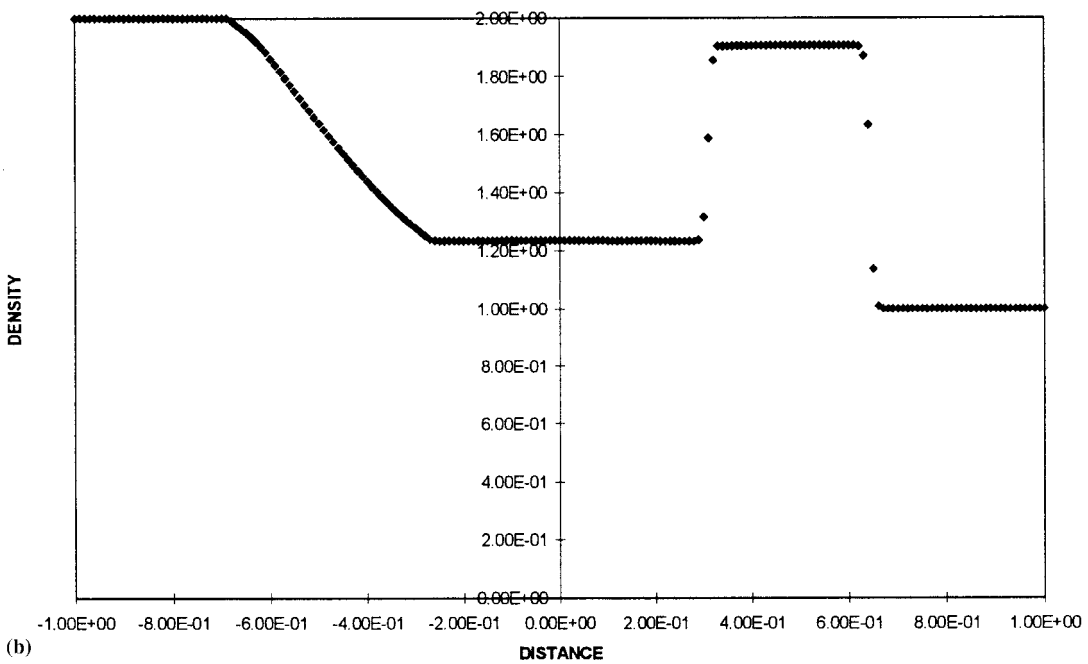

Figure 1. (a) The density profile obtained with Harten's TVD scheme for the shock tube problem; (b) the density profile obtained with the modified Harten's TVD scheme for the shock tube problem.

direction, but they keep decreasing continuously with time (see Figures 2(b) and 3(b)). It may also be noted that after $t' = 140$ μs (i.e. when the pressure at the origin is lower than that at the tail of the rarefaction wave), the second shock ceases its previous outward motion and starts to move inwards, with increasing strength, and finally converges at the center. The

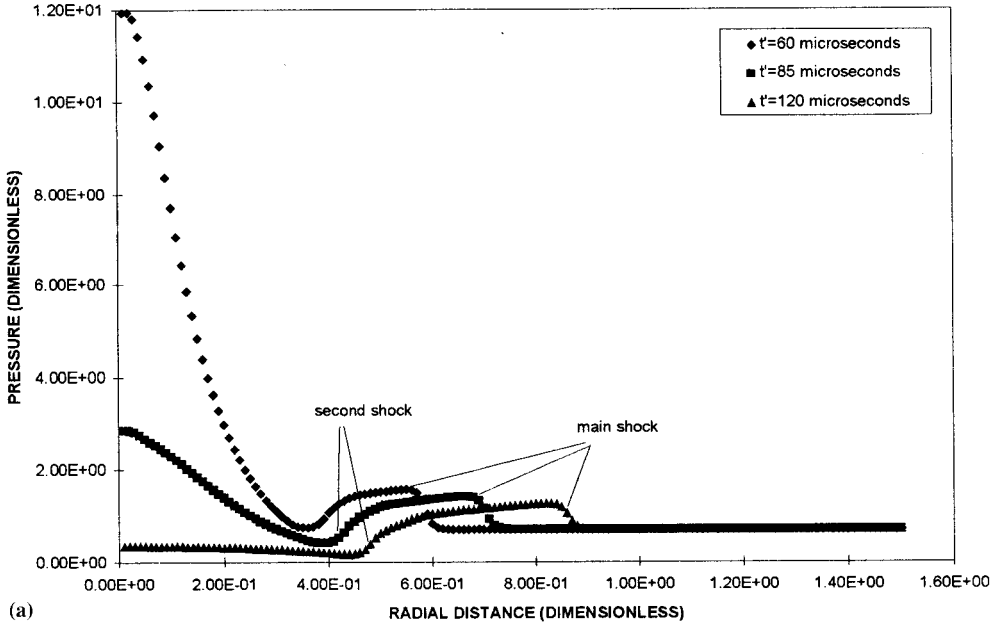

(a)

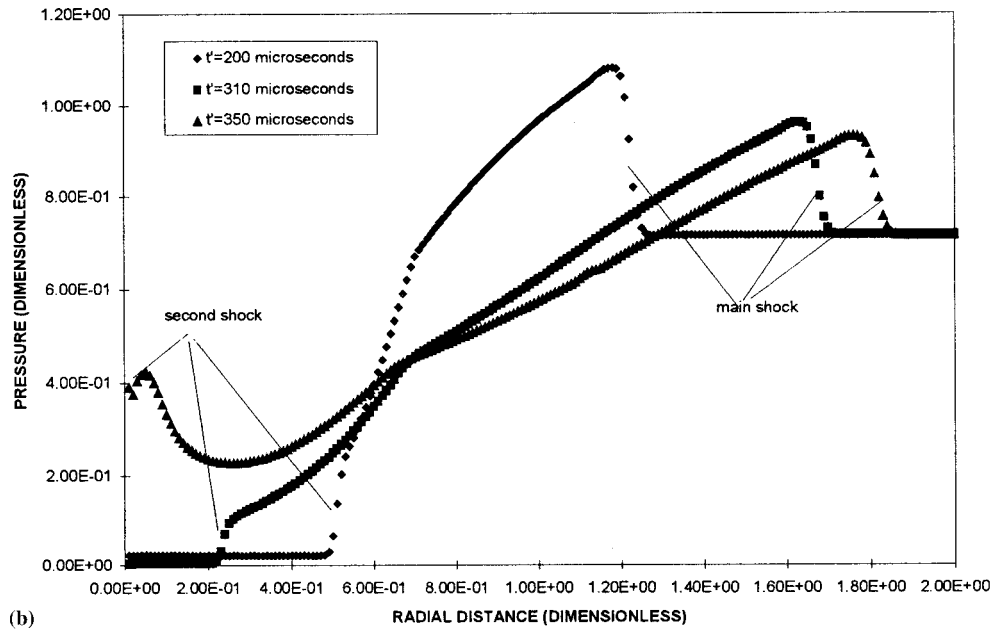

(b)

Figure 2. (a)–(c) The pressure profiles for a spherical explosion centered at the origin.

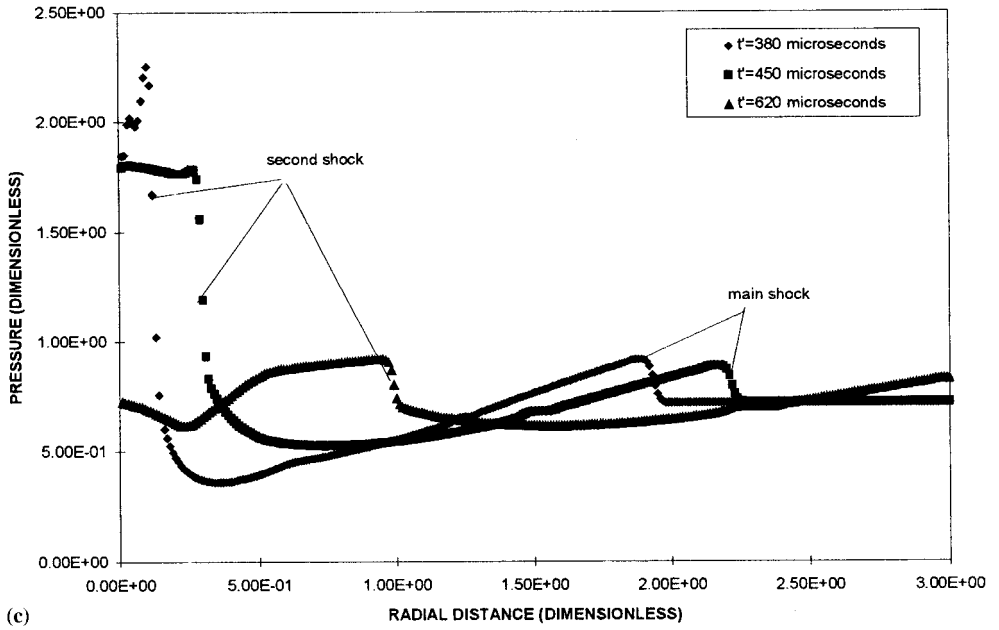

Figure 2 (*Continued*)

implosion of the second shock wave causes a sharp increase of density, pressure and temperature near the explosion center. This occurs at about $t' = 360$ μs. Probably because of numerical viscosity the maximum pressure is less than that of the initial state, unlike the result

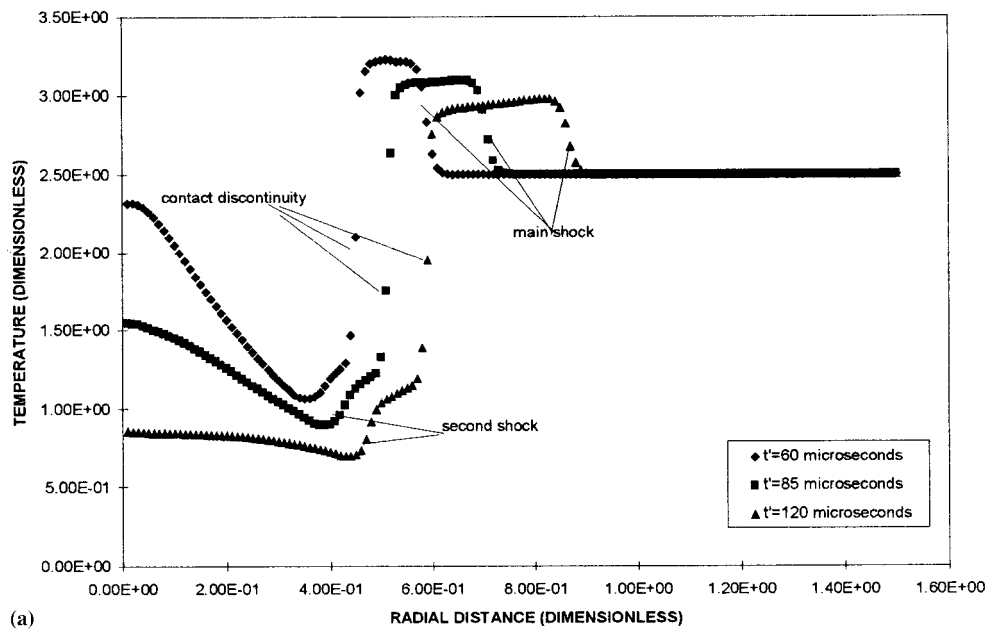

Figure 3. (a)–(c) The temperature profiles for the spherical explosion centered at the origin.

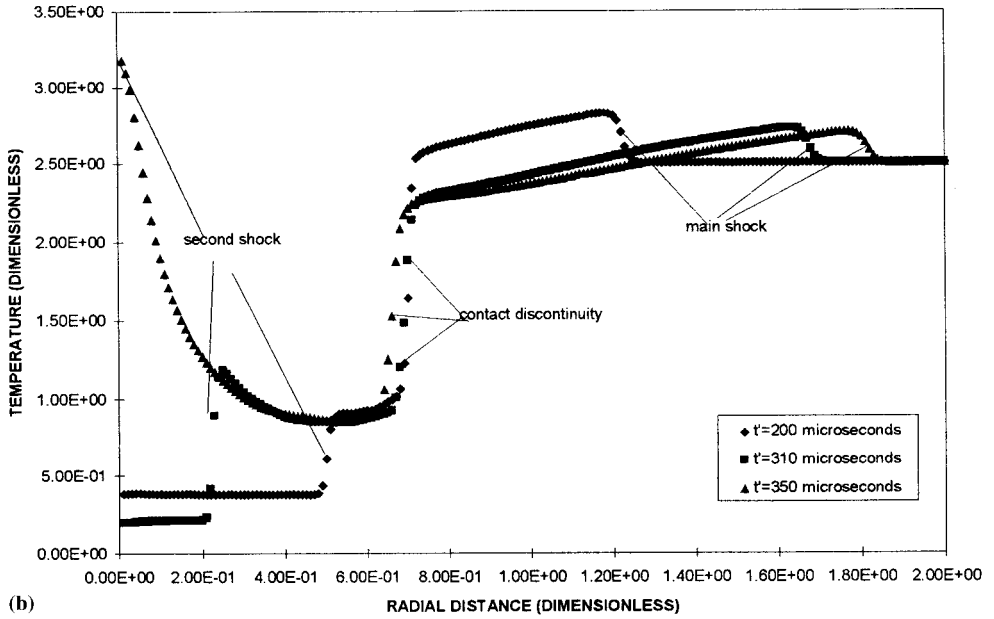

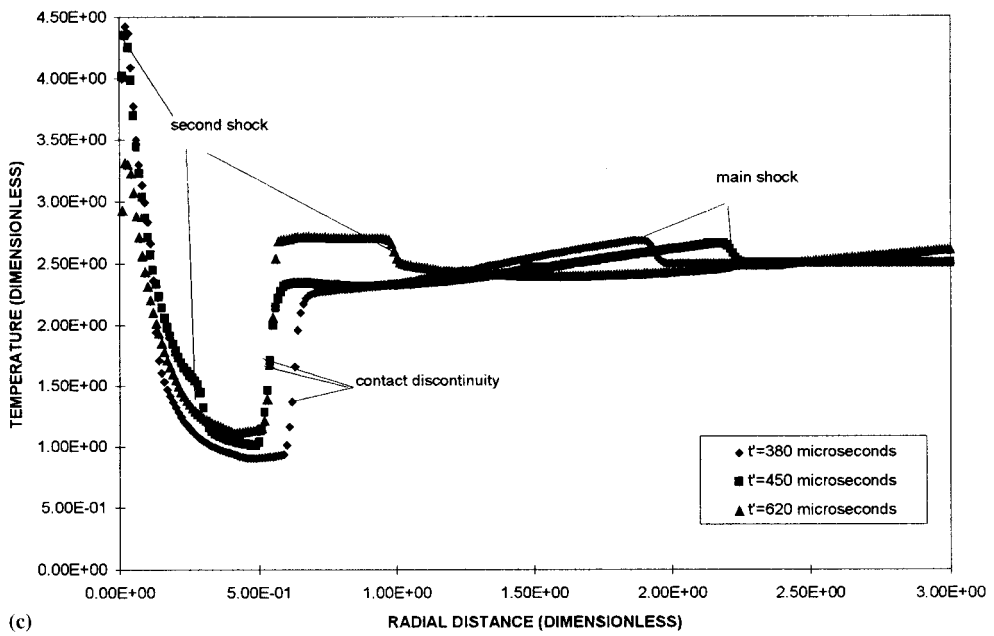

Figure 3 (*Continued*)

of theoretical analysis, which predicts the pressure there could reach infinity for inviscid flow. In Figure 2(c), the pressure at the explosion center decreases again with the radial divergence of the reflected second shock wave.

The temperature profiles are shown in Figure 3(a)–(c). There is an interesting phenomenon about the position of the maximum temperature. After an explosion, the maximum temperature remains at the contact discontinuity till about 100 μs. Beyond that time, the temperature immediately behind the main shock is the largest (see Figure 3(a)). However, the temperature immediately behind the second shock wave rises rapidly and soon takes on the maximum value due to the convergence of the second shock wave at the center (see Figure 3(b)). At $t' = 360$ μs, the second shock wave implodes, resulting in maximum temperature at the origin. Even after the reflected second shock wave propagates radially outwards through the contact discontinuity, the temperature at the center still maintains its maximum value. It probably remains so until the whole flow region becomes uniform. This can be seen in Figure 3(c).

The curves of the discontinuities and their comparison with the results analyzed by Brode [2] are shown in Figure 4(a). From the evolution of the second shock, it can be seen that the latter initially moves away from the origin. At $t' = 170$ μs, the second shock wave ceases its outward motion and begins to move back, and then it implodes on the origin at 360 μs. Because of the inward motion of the second shock wave, the flow behind the second shock wave moves back to the origin, and this results in the contact discontinuity ceasing its outward motion and beginning to move inwards at 240 μs. At about 550 μs, the incoming contact surface meets with the out-going reflected second shock wave and interacts with it, resulting in the slight outward motion of the contact discontinuity and the transmission of the second shock wave. After the second shock is transmitted through the contact discontinuity, the contact discontinuity seems to stay relatively still at the same position. The authors did not obtain the reflection of the second shock at the contact discontinuity surface, probably because the reflection is very weak. In Figure 4(a), the curves marked with open symbols are the analytical ones presented by Brode [2]. The present numerical results certainly show fairly good agreement with those predicted analytically with a maximum deviation limited to less than about 5%.

In Figure 4(b), the present results are compared with those obtained experimentally by Boyer [1]. Except at the initial stage of the explosion, where there is fair agreement of results with the maximum difference limited to less than 13%, the respective results indicate increasing divergence, although it must be stated that both sets of results still exhibit similar trends. Though there are several difficulties associated with the experiment, such as accurate measurements and the need to initiate the 'explosion' as symmetrically as possible, the experiment nevertheless clearly demonstrated the main features of the explosion, like the presence and implosion of the second shock wave. The possible comparison is significant in that such an experiment is rather uncommon and data are not always available in the open literature. From Figure 4(b), it is observed that the time of implosion of the second shock wave at the center occurred later than that obtained numerically; the difference is about 180 μs (i.e. 50%) and the contact discontinuity in the experiment did not indicate any radially inward movement before its interaction with the reflected second shock wave. Closer examination of the shadowgraphs from which the experimental data were deduced reveals three possible causes for the discrepancies observed. One, the thin spherical glassy diaphragm may not have broken instantaneously and, as a result, the flow is not completely spherically symmetric. This asymmetry can contribute to the time delay of implosion of the second shock wave at the center. Besides, difficulties also arise in determining the exact moment at which the second shock front implodes at the center since it is not entirely spherical in shape. The second possible cause is the issue of energy loss in the flow system due to the moving fragments of glass diaphragm. Although the kinetic energy loss can be partly mitigated by equivalently increasing the pressure in the sphere, the loss due to the thermal energy residing in each fragment is not considered.

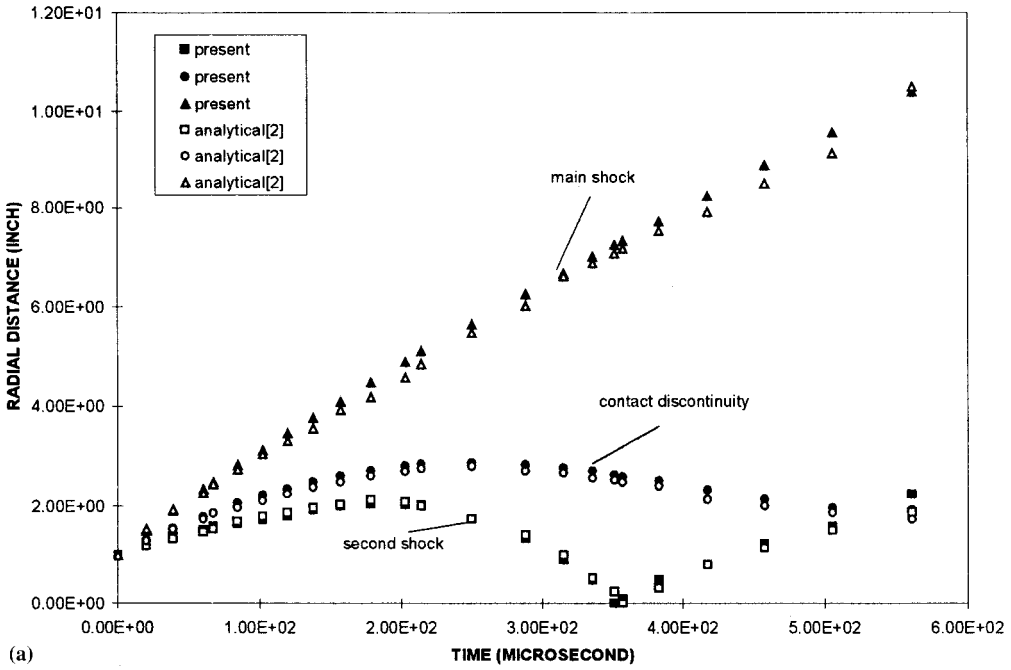

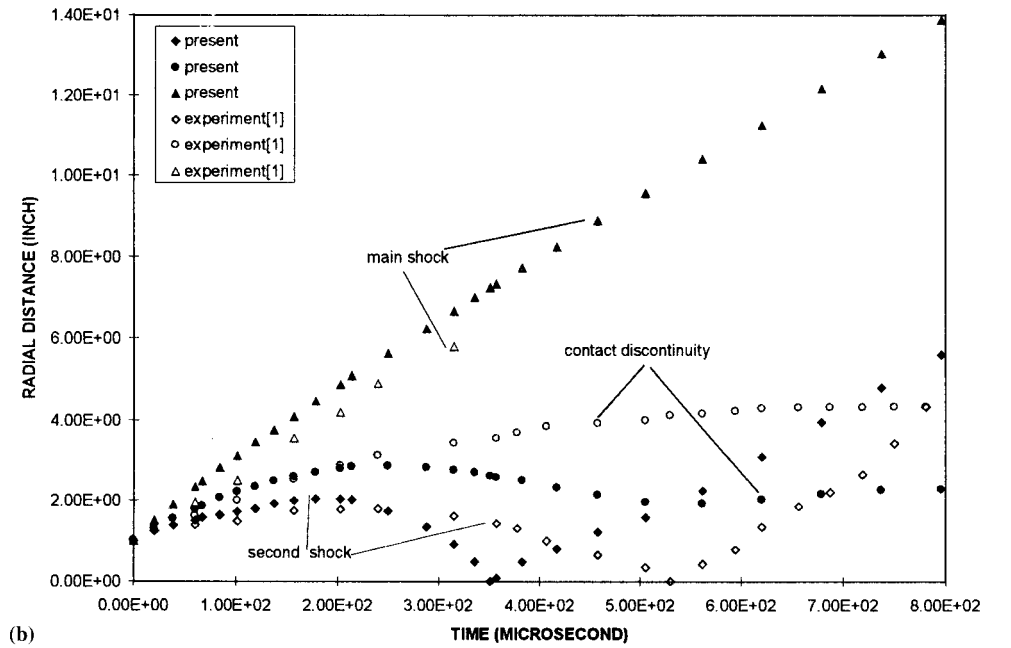

Figure 4. (a) Comparison of the discontinuity systems with the analysis by Brode [2] for the spherical explosion; (b) comparison of the discontinuity systems with the experiments by Boyer [1] for the spherical explosion.

Lastly, the fragments are made of much denser material compared with the surrounding gaseous medium and have much greater inertia; the effect of the slower moving fragments in the flow and across the contact discontinuity may greatly contribute to the asymmetry of the flow.

A cylindrical explosion in air has also been carried out under the same initial conditions as that for the spherical explosion. The numerical simulation shows that the cylindrical explosion shares similar physical attributes as those of the spherical explosion. However, the strength of the second shock in the cylindrical explosion is less than that in the spherical explosion, and its implosion on the origin occurs later than that in the spherical explosion by about 250 μs. Figure 5 summarizes the curves of discontinuities for both the cylindrical and spherical explosions. From Figure 5, the interaction of the second shock wave and contact discontinuity also occurs much later for the cylindrical explosion. It may also be noted that the strength of the main cylindrical shock wave is lower than that of the spherical explosion.

4.2. The numerical simulation of cylindrical implosion

The computation of a cylindrical implosion generated by simultaneously breaking a cylindrical diaphragm, which separates an outer high pressure gas region from an inner low pressure gas cylinder, was carried out by several researchers like Sod [11], Abarbanel and Goldberg [20], Lapidus [21] and Payne [22]. For the sake of further comparison with the computation based on the modified TVD scheme, the present authors shall choose the same model as Sod [11]. The initial non-dimensional conditions are $p_H = 4.0$, $\rho_H = 4.0$, $u_H = 0$, $p_0 = 1.0$, $\rho_0 = 1.0$ and $u_0 = 0$, and the diaphragm is located at 0.25.

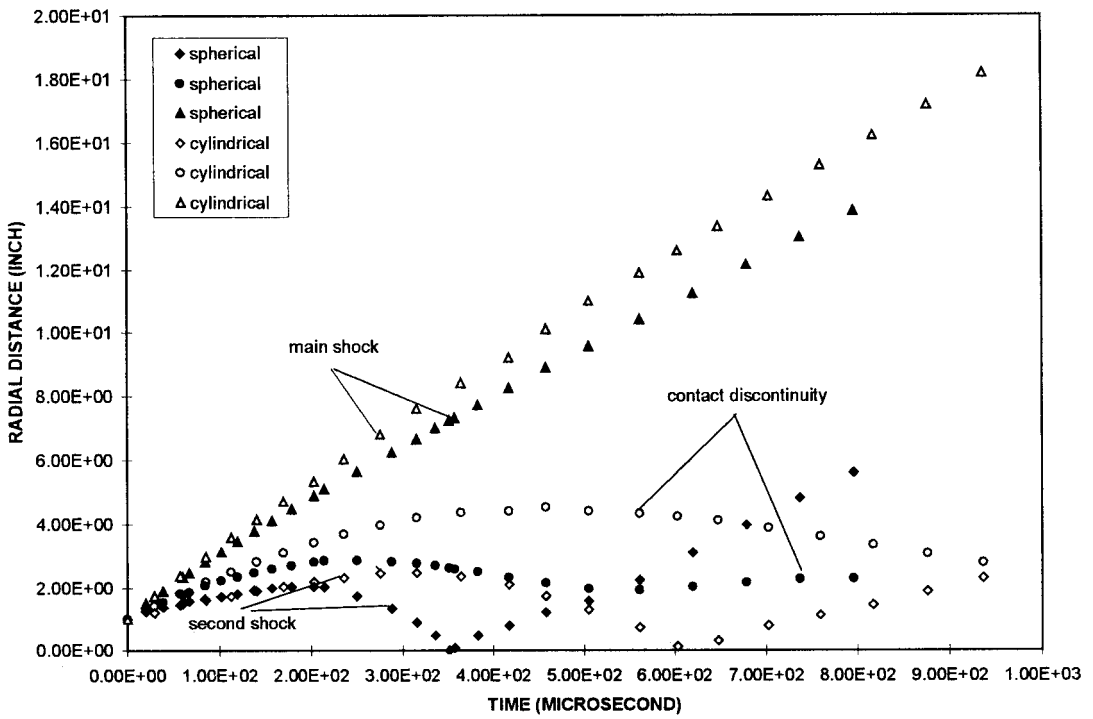

Figure 5. Comparison of the discontinuity systems between a spherical and cylindrical explosions centered at the origin.

When the diaphragm is suddenly broken, there is an inward converging shock wave (called the main shock wave) in the low pressure region, a rarefaction wave moving out into the high pressure region with a moving-in contact discontinuity separating the rarefaction wave and the main shock wave. In Figure 6(a), the pressure profiles at five stages are displayed. This figure

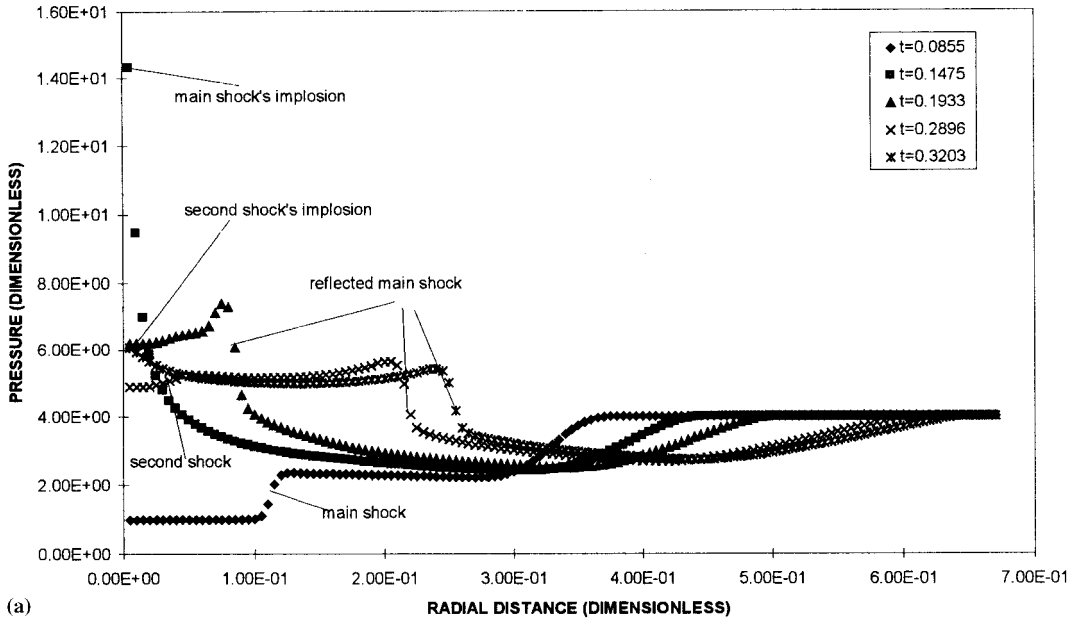

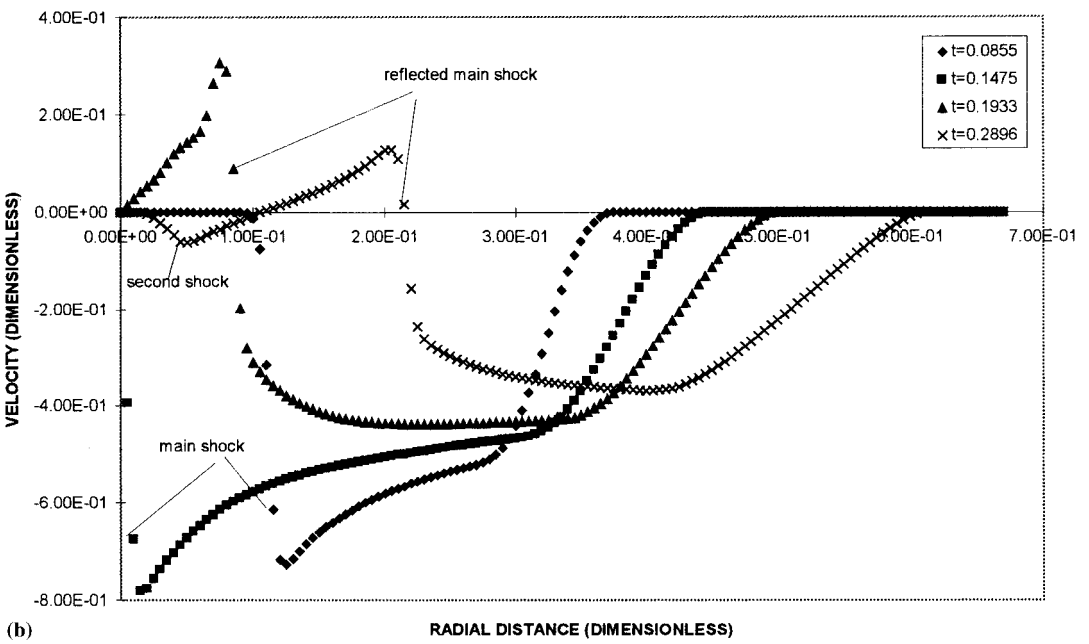

Figure 6. (a) The pressure profiles for a cylindrical implosion centered at the origin; (b) the velocity profiles for the cylindrical implosion centered at the origin; (c) the density profiles for the cylindrical implosion centered at the origin.

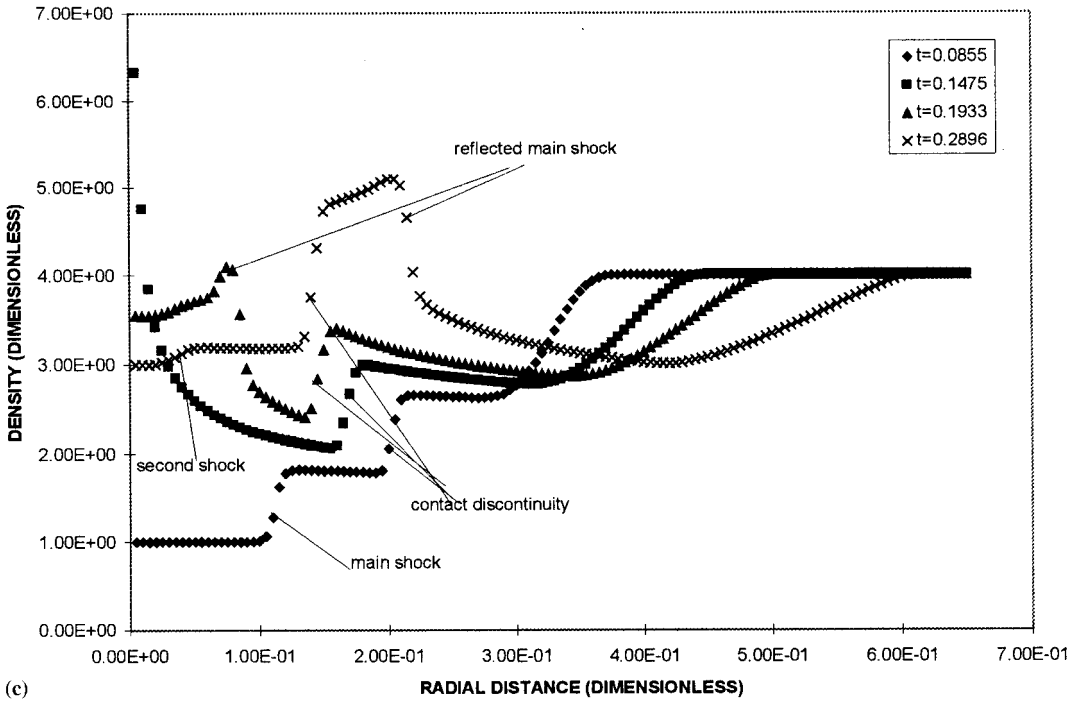

Figure 6 (*Continued*)

shows that the shock wave with increasing strength converges on the origin at about $t = 0.15$, which is in good agreement with that computed by Sod [11]. Because of the implosion, the pressure increases rapidly to a large but finite value. The temperature and density at the center also attain their maximum values at the same time. After its implosion, the main shock wave is reflected outwards and results in a decrease of pressure. The out-going main shock wave, after a certain time period, begins to interact with the incoming contact discontinuity front, thereby causing the contact discontinuity to remain stationary in space (see below for more details). In the meantime, part of the main shock front is transmitted and the other portion is reflected at the contact discontinuity. The pressure plot in Figure 6(a) at $t = 0.2896$ indicates a reflected shock (which is called the second shock wave), albeit a relatively weak one, at the position of about $r = 0.05$. At $t = 0.32$, the moving-in second shock wave converges at the center and causes the pressure there to increase again.

In Figure 6(b), the velocity plot is shown for the same time histories as in Figure 6(a). The trend is rather similar to that of the pressure plot. Behind the converging main shock front, the velocity assumes a negative value (i.e. moving radially inwards) and shows a rapid increase in magnitude with time. After its implosion at the center, the main shock wave diverges radially out and results in a decreasing positive velocity behind it. Due to the reflection of the main shock wave at the contact discontinuity (at $t = 0.2896$), a moving-in second shock appears in the velocity profile and the associated velocity behind it is negative.

The density profiles displayed in Figure 6(c) exhibit evolution of the contact discontinuity. It shows the same characteristic trends for the main and second shock waves as those displayed in the pressure and velocity profiles. The contact discontinuity first moves inwards and subsequently ceases its inward motion due to the impingement of the reflected main shock

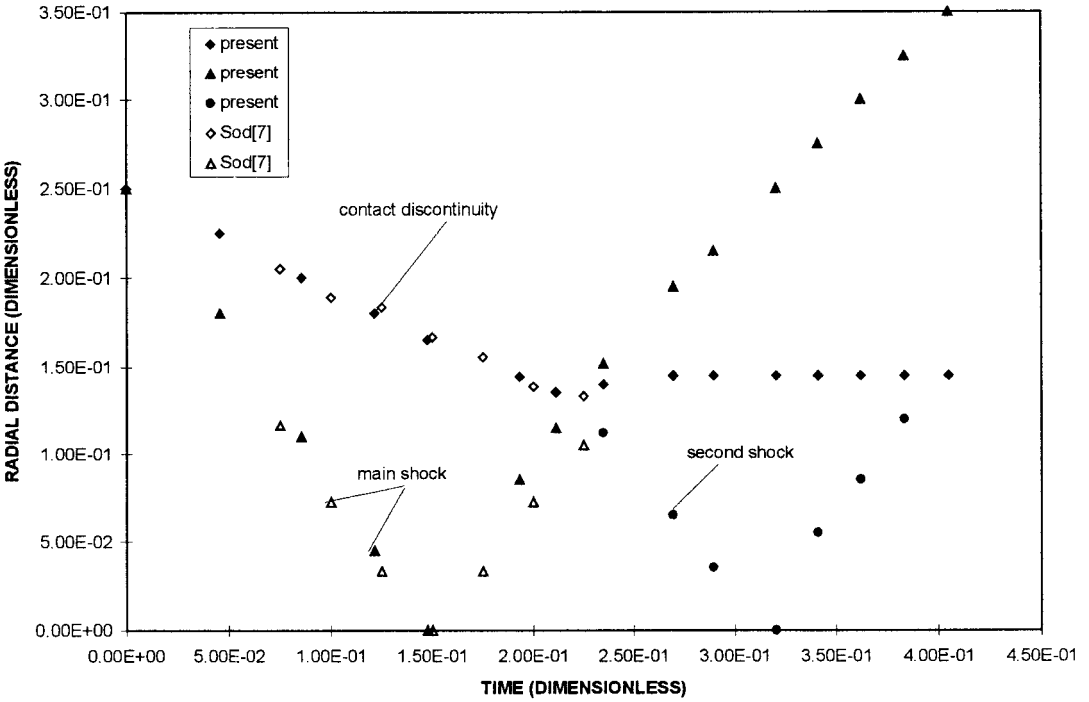

Figure 7. Comparison of the discontinuity systems for the cylindrical implosion centered at the origin.

wave, and finally stays more or less at rest. It can be further observed from Figure 6(c) that the magnitude of density immediately behind the contact discontinuity front increases continuously with time until the reflected main shock wave meets the contact discontinuity. At $t = 0.2896$, the reflected main shock wave has been transmitted through the contact discontinuity and diverges out with decreasing strength. It can also be observed that the contact discontinuity is always sharp.

The portion of contact discontinuities in the cylindrical implosion and their comparison with the results computed by Sod [11] are shown in Figure 7. From this figure, the initially moving-in main shock front converges at the center at $t = 0.15$ and is reflected; then the out-going reflected main shock meets the converging contact discontinuity at $t = 0.22$, resulting in its transmission through the contact discontinuity front and the generation of the second shock wave. Due to the interaction of the main shock front with the contact discontinuity, the latter ceases its inward motion and moves slightly outwards and, finally, stays at rest. The inward-moving second shock front converges at the center at $t = 0.32$ and is reflected. In Figure 7, the open symbols, which pertain to the main shock front and contact discontinuity, were obtained by Sod [11] using Glimm's scheme; the second shock wave computed with Glimm's scheme is not shown as there are insufficient data as deduced from the paper [11]. The current results show fair agreement with those computed by Sod except for the slight divergence of the position of the main shock after its reflection at the center. It may be noted that Glimm's scheme is strictly first-order-accurate and Sod did not attempt to compare his results with other data, whether experimental or otherwise, to establish accuracy. Overall, the maximum deviation between the results is limited to less than 10% (in terms of magnitude) and the trends obtained are in full agreement. This comparison with Sod's work is also significant in that the latter is based on the completely different Glimm's scheme.

The results in Figure 6(a)–(c) indicate that both the main and second shock waves and contact discontinuity are captured successfully with the modified TVD scheme. This is especially significant since the second shock wave was not clearly captured by the previous works of Abarbanel and Goldberg [20], Lapidus [21] and Payne [22]. Furthermore, in the current results, the contact discontinuity remains highly resolved, unlike that produced by Payne's method, which was quite smeared out.

Finally, the mechanism for the generation of the second shock wave in the cylindrical implosion problem should theoretically be the same as that for the generation of the third shock wave as discussed in the previous section. The current scheme is not able to indicate clearly the presence of the third shock wave; the previous works [20–22] did not show its presence not to mention the occurrence of the second shock. One reason is that the third shock is physically so weak and occurs so late that it is extremely difficult for a numerical scheme to detect. Another factor could be the modified TVD scheme may still not be sufficiently sensitive to capture this very weak third shock front. (Harten's TVD scheme is also unable to capture the third shock front, not shown.) On the other hand, the present method has clearly demonstrated many useful features in capturing faithfully the second shock front and highly resolving the contact discontinuity.

5. CONCLUSION

In this paper, the numerical study of the explosion generated by a pressurized air sphere or cylinder is carried out using the modified Harten's TVD scheme, which incorporates the ACM technique for application to the contact discontinuity region. The second shock wave and its subsequent implosion on the origin are captured, and the curves of the discontinuities have shown good agreement with those predicted analytically. There is also fair concurrence of results with experiments especially at early times; although there are larger discrepancies observed for the various quantities at later times, the trends obtained are identical. A cylindrical explosion under the same initial conditions as for spherical explosion is also carried out and the differences between the spherical explosion and the cylindrical explosion are analyzed and discussed.

Using the same modified TVD scheme, the numerical simulation for a cylindrical implosion problem has also been performed. All the primary features of the implosion are obtained and the results are discussed and compared with those obtained using Glimm's scheme.

Overall, the modified Harten's TVD scheme used is able to obtain the high resolution of the contact discontinuity and enables the main and second shock fronts to be successfully captured for an explosion or implosion problem.

APPENDIX A

Because the term $g_j^l = (1 + q_{j+1/2}^l) g_j^{H,l}$ can be regarded as one order higher than $g_j^{H,l}$ used in the original Harten's TVD scheme [12], the former satisfies the condition put forth as Lemma 3.2 in the original Harten paper [12]. Furthermore, $H_{j=1/2}^n$ in Equation (3.1a) is a second-order approximation of the numerical flux of the second-order Lax–Wendorff scheme. Therefore, the overall numerical scheme (3.1) is second-order-accurate and conservative. As for the TVD feature of scheme (3.1), it shall be analyzed for the linear Euler equation system as similarly carried out in Harten's paper [12]. Recall that a scalar conservative scheme can be rewritten as

$$U_j^{n+1} = U_j^n + C_{+,j+1/2}\Delta_{j+1/2}U - C_{-,j-1/2}\Delta_{j-1/2}U, \tag{A.1}$$

and scheme (A.1) will be TVD if $C_{\pm,j+1/2} \geq 0$ and $C_{+,j+1/2} + C_{-,j+1/2} \leq 1$. Since a linear Euler equation system can be uncoupled into several scalar equations and $C^l_{\pm,j+1/2}$ is obviously not negative for the present scheme (3.1), there is need only to show that

$$C^l_{+j+1/2} + C^l_{-j+1/2} \leq 1$$

is satisfied. The term $C^l_{\pm,j+1/2}$ takes on the same definition as in Harten's paper [12]. The authors shall start from the expression

$$C^l_{+,j+1/2} + C^l_{-,j+1/2} = \varphi(v^l_{j+1/2} + r^l_{j+1/2}). \tag{A.2}$$

From the right-hand-side of Equation (A.2)

$$|r^l_{j+1/2}| = \frac{|g^l_{j+1} - g^l_j|}{|\alpha^l_{j+1/2}|} \leq \frac{\max(|g^l_{j+1}|, |g^l_j|)}{|\alpha^l_{j+1/2}|} \leq (1 + q^l_{j+1/2})\sigma(v^l_{j+1/2}), \tag{A.3}$$

where $v^l_{j+i/2} = \xi_r \lambda^l_{j+1/2}$ and

$$q^l_{j+1/2} = S_{j+1/2} \times \frac{|\alpha^l_{j+1/2} - \alpha^l_{j-1/2}|}{|\alpha^l_{j+1/2}| + |\alpha^l_{j-1/2}|} \times \frac{\varphi(v^l_{j+1/2})}{\sigma(v^l_{j+1/2})} \leq \frac{\varphi(v^l_{j+1/2})}{\sigma(v^l_{j+1/2})},$$

therefore

$$\varphi(v^l_{j+1/2} + r^l_{j+1/2}) \leq |v^l_{j+1/2}| + |r^l_{j+1/2}| \leq |v^l_{j+1/2}| + \sigma(v^l_{j+1/2}) + \varphi(v^l_{j+1/2}), \tag{A.4}$$

i.e.

$$\varphi(v^l_{j+1/2} + r^l_{j+1/2}) \leq \frac{5}{2}|v^l_{j+1/2}| - \frac{1}{2}|v^l_{j+1/2}|^2. \tag{A.5}$$

If $\frac{5}{2}|v^l_{j+1/2}| - \frac{1}{2}|v^l_{j+1/2}|^2 \leq 1$, then we have $C^l_{+,j+1/2} + C^l_{-,j+1/2} \leq 1$. This is only true when $|v^l_{j+1/2}|$ is less than or equal to $(5 - \sqrt{17})/2$.

REFERENCES

1. D.W. Boyer, 'An experimental study of the explosion generated by a pressurized sphere', *J. Fluid Mech.*, **9**, 401–429 (1960).
2. H.L. Brode, 'Theoretical solutions of spherical shock tube blasts', *The RAND Corporation*, *RM-1974*, 1957.
3. M.P. Friedman, 'A simplified analysis of spherical and cylindrical blast waves', *J. Fluid Mech.*, **11**, 1–15 (1961).
4. I.I. Glass, *Nonstationary Flows and Shock Waves*, Oxford Science Publications, Oxford, 1994.
5. W.E. Baker, *Explosions in Air*, Wilfred Baker Engineering, San Antonio, 1973.
6. J. Flores and M. Holt, 'Grimm's method applied to underwater explosions', *J. Comput. Phys.*, **44**, 377–387 (1981).
7. C. Shu, Private communication, Department of Mechanical Engineering, National University of Singapore, 1996.
8. P. Charrier and B. Tessieras, 'A front-tracking method applied to hyperbolic systems of nonlinear conservation laws', *SIAM J. Numer. Anal.*, **23**, 461–472 (1986).
9. J. Falcovitz and A. Birman, 'A singularities tracking conservation laws scheme for compressible duct flows', *J. Comput. Phys.*, **115**, 431–439 (1994).
10. M. Ben-Artzi and J. Falvovitz, 'A second-order Godunov-type scheme for compressible fluid dynamics', *J. Comput. Phys.*, **55**, 1–32 (1984).
11. G.A. Sod, 'A numerical study of a converging cylindrical shock', *J. Fluid Mech.*, **83**, 785–794 (1977).
12. A. Harten, 'High resolution schemes for hyperbolic conservation laws', *J. Comput. Phys.*, **49**, 357–393 (1983).
13. A. Harten, B. Engquist, S. Osher and S. Chakravarthy, 'Uniformly high-order-accurate essentially non-oscillatory scheme III', *J. Comput. Phys.*, **71**, 231–303 (1987).
14. C.W. Shu and S. Osher, 'Efficient implementation of essentially non-oscillatory shock-capturing schemes II', *J. Comput. Phys.*, **83**, 32–78 (1989).
15. A. Harten, 'The artificial compression method for computation of shocks and contact discontinuities: I. Single conservation laws', *Comm. Pure Appl. Math.*, **30**, 611–638 (1977).
16. A. Harten, 'ENO scheme with subcell resolution', *J. Comput. Phys.*, **83**, 148–384 (1989).

17. Mao De-Kang, 'A shock tracking technique based on conservation in one space dimension', *SIAM J. Numer. Anal.*, **32**, 1677–1703 (1995).
18. Huanan Yang, 'An artificial compression method for ENO schemes: the slope modification method', *J. Comput. Phys.*, **89**, 125–160 (1990).
19. A. Harten, 'The artificial compression method for computation of shocks and contact discontinuities: III. Self-adjusting hybrid schemes', *Math. Comput.*, **32**, 363–389 (1978).
20. S. Abarbanel and M. Goldberg, 'Numerical solution of quasi-conservative hyperbolic system—the cylindrical shock problem', *J. Comput. Phys.*, **10**, 1–33 (1972).
21. A. Lapidus, 'Computation of radially symmetric shocked flows', *J. Comput. Phys.*, **8**, 106–140 (1971).
22. R.B. Payne, 'A numerical method for a converging cylindrical shock', *J. Fluid Mech.*, **2**, 185–200 (1956).

